# An Exploration of the Role of Transient Eddies in Determining the Transport of a Zonally Reentrant Current

ROBERT HALLBERG

*NOAA/Geophysical Fluid Dynamics Laboratory, Princeton, New Jersey*

ANAND GNANADESIKAN

*Atmospheric and Oceanic Sciences Program, Princeton University, Princeton, New Jersey*

ABSTRACT

The meridional Ekman transport in a zonally reentrant channel may be balanced by diabatic circulations, standing eddies associated with topography, or by Lagrangian mean eddy mass fluxes. A simple model is used to explore the interaction between these mechanisms. A key assumption of this study is that diabatic forcing in the poleward edge of the channel acts to create lighter fluid, as is the case with net freshwater fluxes into the Southern Ocean. For weak wind forcing or strong diabatic constraint, a simple scaling argument accurately predicts the level of baroclinic shear. However, given our understanding of the relative magnitudes of Ekman flux and deep upwelling, this is not the appropriate parameter range for the Antarctic Circumpolar Current. With stronger wind stresses, eddies are prominent, with baroclinic instability initially developing in the vicinity of large topography. Arguments have been advanced by a number of authors that baroclinic instability should limit the velocity shear, leading to a stiff upper limit on the transport of the current. However, in the simulations presented here baroclinic instability is largely confined to the region of topographic highs, and the approach to a current that is independent of the wind stress occurs gradually. Several recent parameterizations of transient eddy fluxes do not reproduce key features of the observed behavior.

## 1. Introduction

The Antarctic Circumpolar Current (ACC) is the world's strongest ocean current with a transport of 130–150 Sv (Whitworth et al. 1982; Orsi et al. 1995). However, no comprehensive theory exists for relating the transport of the ACC to the large-scale wind and buoyancy forcing. A large number of studies have attempted to construct such theories by focusing on the zonal momentum balance. Idealized studies have unambiguously demonstrated that some combination of transient eddies and standing eddies linked with large-scale bottom topography can transmit zonal momentum downward through the stratified water column (McWilliams et al. 1978; Treguier and McWilliams 1990; Wolff et al. 1991). Integrated through the water column, zonal surface stresses may then be balanced by form drag over bottom topography, as first suggested by Munk and Palmén (1951). In the limit that transient eddy fluxes are important, the necessary condition for baroclinic instability that meridional potential vorticity gradients must

vanish somewhere in the water column might be expected to lead to weak potential vorticity gradients throughout much of the water column (Marshall et al. 1993; Straub 1993). The transport of the ACC can then be estimated, provided that the stratification to the north of the ACC is known.

Other theories for the transport of the ACC note that the current flows over such large-amplitude topography that all contours of the barotropic potential vorticity $f/H$ (where $f$ is the Coriolis parameter and $H$ is the water depth) intersect the ocean boundaries. (More precisely, these contours all pass within a hypothesized viscous or turbulent boundary layer over the continental slopes.) If the stratification is assumed to only partially shield the surface flow from the topography and the path for the ACC is assumed to be fixed, the transport of the current can be easily linked to the strength of the winds along critical contours of potential vorticity (see, e.g., Wang 1994; Wang and Huang 1995; Krupitsky et al. 1996).

These theories, however, largely neglect the effects of buoyancy forcing. Gnanadesikan and Hallberg (2000) note that the momentum balance has to be considered within the context of how the density structure of the ACC is maintained, and noted that both local and remote

*Corresponding author address:* Dr. Robert Hallberg, NOAA/Geophysical Fluid Dynamics Laboratory, P.O. Box 308, Princeton, NJ 08542.
E-mail: rwh@gfdl.gov

buoyancy forcing could play a role in setting up the density structure. The ACC has an equivalent barotropic structure (flows do not change direction dramatically, but there is a baroclinic shear that leads to relatively small velocities at the bottom) and the vertical shears of velocity are related to density through the thermal wind equation. The density contrast across the current is thus closely linked to the overall transport. A key difference between the ACC and other current systems is that in the latitudes of Drake Passage the flow is unblocked by topography above a depth of about 2000 m. Westerly winds in these "open" latitudes drive a northward Ekman transport of light Antarctic surface water. Geostrophic flows (associated with the ocean imparting eastward angular momentum to the solid earth) result in a net southward velocity, averaging along geopotential surfaces, of the dense waters below the depth of several ridges that span the passage. These flows must be balanced if the density structure (and by implication the circumpolar current) are to remain in steady state. As shown in Fig. 1, there are three possible means of maintaining the density structure: through diapycnal fluxes, stationary eddies, and transient eddies. In the real circumpolar current all three processes are probably involved, but it is helpful to consider each one separately.

The first way to maintain the pool of light surface water within the Southern Ocean is to convert dense water into light water. In the Southern Ocean, this may be accomplished by upwelling dense water from below, freshening it, and then warming it as it is moved northward. This light water must then be converted back to dense water farther north. In coarse-resolution general circulation models, this process plays an important role in setting the thermal structure of the global ocean (Gnanadesikan 1999; Gnanadesikan and Hallberg 2000; Gent et al. 2001). The transport of the circumpolar current is then determined by the relationship between the density structure and the buoyancy forcing. In the coarse models, increases in the pycnocline depth to the north of the current are associated with an increase in the magnitude of overturning and buoyancy fluxes in the Northern Hemisphere. Thus, if the winds are increased in the south, the pycnocline depth increases in the north until the increased transformation of light water to dense water in the north balances the increased transformation of dense water to light water in the south. This in turn increases the thermal wind shear within the circumpolar current and the transport of the current as a whole (Gnanadesikan and Hallberg 2000).

The second method for replenishing the light water is to return it at intermediate depths as a geostrophic flow (Fig. 1b). In this picture the surface water is subducted to the north of Drake Passage and returns in those regions where the circumpolar current drifts southwards. Geostrophic flows in the upper layer are directed northward in thin layers (generally over topography) and southward in thicker layers (generally where the bottom

is deeper). This picture assumes an important role for topography since the meanderings of the circumpolar current are closely connected with topographic features such as the Scotia Arc, Kerguelen Ridge, and the Campbell Plateau (Gille 1997; Witter and Chelton 1998). The plausibility of these stationary eddies balancing the Ekman transport has been amply demonstrated in eddy-resolving idealized studies (McWilliams et al. 1978; Wolff et al. 1991) and in coarser, more realistic simulations (Killworth and Nanneh 1994). It is not clear from this picture whether the transport in the circumpolar current should increase with increasing winds or whether it should become saturated. Olbers and Völker (1996) and Völker (1999) propose that the ACC accelerates until the first baroclinic mode becomes trapped over topography, generating large stationary eddies. These stationary eddies then produce an "internal form stress" in which there is a net pressure force across an isopycnal surface corresponding to a vertical flux of horizontal momentum.

The third method for replenishing the light water is to return it southward as a Stokes drift associated with transient eddies (Straub 1993; Marshall et al. 1993; Tansley and Marshall 2001). Transient eddies can produce an interfacial form stress that fluxes momentum in the vertical. As with the stationary interfacial form stress this involves an upper-level flow field in which thin columns are advected northward, while thick columns are advected southward. As illustrated in Fig. 1c, the reverse flow field is found in the lower layer. Proponents of this idea argue that the ACC accelerates until it becomes baroclinically unstable. At that point baroclinic eddies develop and generate mass transports that counteract the Ekman transport and deep geostrophic flows.

The stationary and transient eddies may be quite closely linked. Treguier and McWilliams (1990) note that, while the standing eddy form stress is of leading order importance in distributing zonal momentum downward in the water column, strong viscosity or transient eddies are required to transmit energy downward in an adiabatic system. Also, transient eddies may be instrumental in maintaining the time-mean flow field that provides the stationary eddy form stress.

In the real world, all three processes probably play a role. As pointed out by a number of authors (Warren et al. 1996; Wunsch 1998; Toggweiler and Samuels 1998; Gnanadesikan 1999) the net buoyancy flux in the Southern Ocean acts to lighten water, and there is certainly a northward flow of Antarctic Intermediate Water out of the Southern Ocean (Schmitz 1995; Macdonald 1998; de las Heras and Schlitzer 1999). However, this diapycnal cell is unlikely to be the only process involved. The estimates for the formation rate of Antarctic Intermediate Water range between 14 and 26 Sv (Sv $\equiv 10^6$ m$^3$ s$^{-1}$), while estimates of the northward Ekman transport in the mixed layer are between 30 and 45 Sv. Even if almost all of the North Atlantic Deep Water upwells in the Southern Ocean as suggested by theory (Gnan-
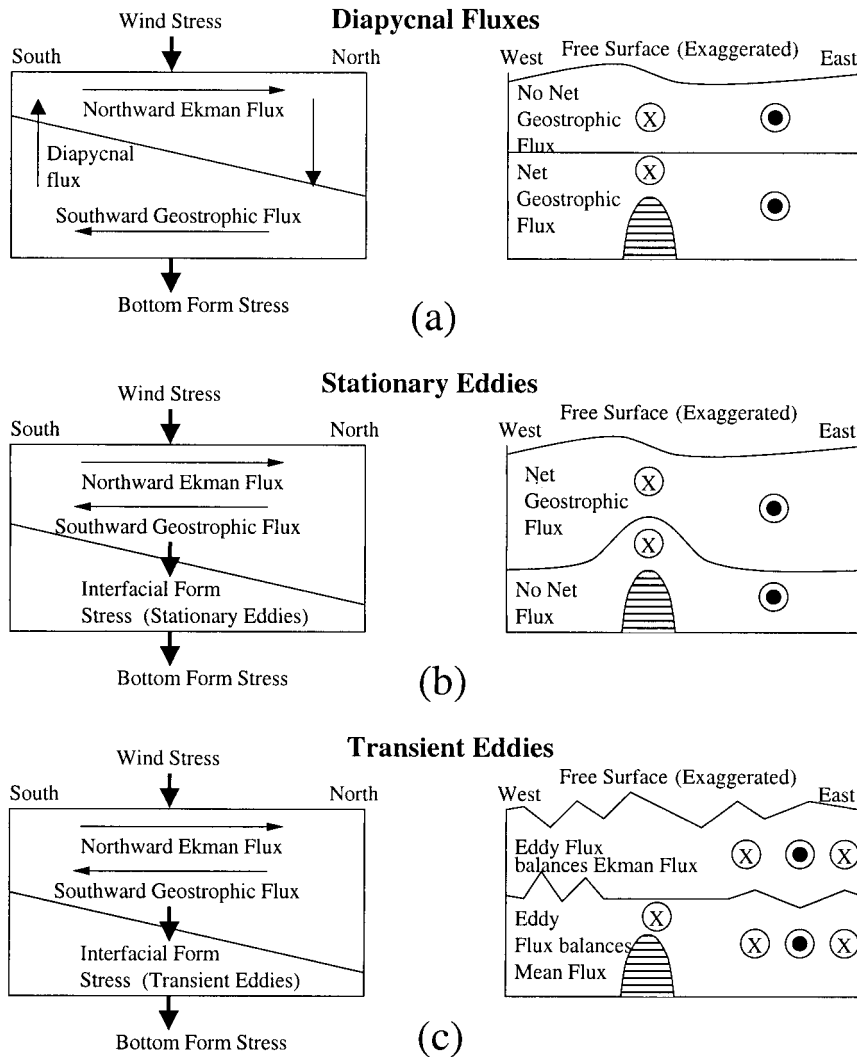
FIG. 1. A conceptual picture of how different physical mechanisms act to maintain the density structure of the Southern Ocean in steady state, given the constant northward flux of light water in the surface layer. (a) **Diapycnal fluxes:** This picture assumes that the light water continuously supplied from below as dense water is upwelled, freshened, and warmed. A counterbalancing transformation must then take place farther north. The dense water is then fed in at depth by geostrophic flows. The resulting momentum balance is one in which bottom form stress balances surface wind stress. (b) **Stationary eddies:** In this case, the transport is balanced in the upper layer as the internal interface deforms to reflect the topography. This creates a situation where northward flows in the upper layer occur in thin layers, while southward flows occur in thick layers. Pressure forces acting on the internal interface result in a form stress that transfers momentum to the lower layer, in which there is no net flow. (c) **Transient eddies:** Instead of stationary eddies accomplishing the transfer of momentum, transient eddies do so.

adesikan 1999) and GCM model experiments (Hirst 1999), some process must still act to return around half of the Ekman transport to the South. Döös and Webb (1994) and Killworth and Nanneh (1994) suggested that stationary eddies played an important role here, noting that when the overturning in the Fine-Resolution Antarctic Model (FRAM) was plotted on density surfaces the apparent volume transport was reduced by half. The model did not, however, fully resolve eddies since the horizontal grid resolution at 60°S was only about 27

km, comparable to the deformation radius. It is thus likely that the FRAM model results underestimated the importance of transient eddies.

This paper presents some simple idealized model experiments in a zonally reentrant channel where the effects of buoyancy forcing, stationary eddies associated with topography, and transient eddies are all present. It explores the transition between a buoyancy-dominated regime, where changes in the wind stress are linearly related to the transport of the mean current, and an eddy-

dominated regime, where changes in the strength of the winds produce changes in both the stationary and transient eddy fields, but relatively little change in the mean transport of the current. The transition between the two regimes is not sharp and the real circumpolar current is arguably in some intermediate range where stationary eddies, baroclinic eddies, and buoyancy forcing all play a role.

## 2. Description of experiments

A series of ocean model simulations are used to explore the relative applicability of the three possible balances for the Ekman transport over a broad range of two key parameters. The intensity of the wind stress (and thus the Ekman transport) is varied by a factor of 4, while the damping timescale associated with the diapycnal circulation is varied by a factor of 16. A total of 15 simulations are compared.

The model itself solves the primitive equations in isopycnal coordinates. The model is similar to that described in Hallberg and Rhines (1996). The Coriolis and momentum advection terms are treated with the scheme of Arakawa and Hsu (1990), which conserves energy and enstrophy in the limit of horizontally nondivergent flow. The continuity equation uses the positive definite scheme of Hsu and Arakawa (1990). The split explicit time stepping scheme is described in Hallberg (1997). Momentum is mixed predominantly through a biharmonic friction term, although a weak vertical viscosity and bottom drag are also applied.

The domain extends for 40° in longitude and 25° in latitude (from 60° to 35°S, and is zonally reentrant. This domain is large enough to admit substantial evolution of the flow downstream of the topography, but is small enough to be computationally affordable at the resolution of these simulations. An additional simulation with the same topography but a domain that extends for 120° in longitude was consistent with the suite of simulations described here.

The bottom is 4000 m deep except for a meridional ridge 1250 m, high with a profile given by

$$H = 4000 \text{ m}$$
$$- 1250 \text{ m} \times [1 - \cos(\pi(\text{lon} - 10°\text{E})/5°)]$$
$$\text{for } 10°\text{E} < \text{lon} \le 20°\text{E} \qquad (1)$$

as depicted in Fig. 2. This topography causes all barotropic potential vorticity ($f/H$) contours to intersect the vertical northern wall, as seen in the dashed contours of Fig. 2. In the real world, all barotropic potential vorticity contours may be effectively blocked in the Southern Hemisphere (Krupitsky et al. 1996), by virtue of all the contours passing within a boundary layer thickness where the planetary geostrophic assumptions (linear, steady, inviscid flow) may be violated, allowing leakage of information between the contours. On the other hand, the intrinsic timescales of barotropic waves may be short
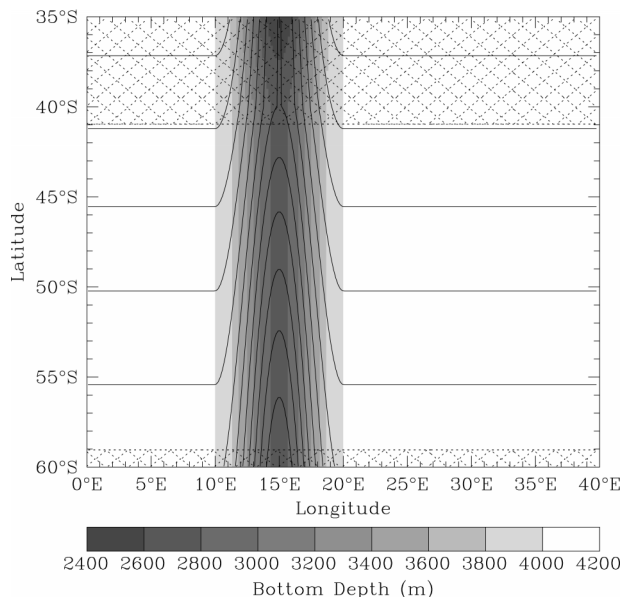


FIG. 2. Plot of topography (shaded), contours of $f$ over the total depth, and diabatic forcing regions (cross hatching) for the model runs.

enough for the description of $f/H$ contours as characteristics to be useful. Hughes et al. (1999) have shown the unblocked $f/H$ contours around Antarctica to be significant for understanding the high-frequency fluctuations in the barotropic transport of the ACC. In any case, the forcing is steady in the idealized experiments presented here, and the choice to avoid open barotropic PV contours frees the barotropic mode from the possibility of an unnaturally strong dependence on the subgrid-scale closure.

The resolution in density space is deliberately coarse, with only two layers. This resolution is adequate to distinguish the dynamical balances in question, and it substantially simplifies the description and analysis of the simulations. The density difference between the layers gives a reduced gravity across the internal interface of 0.0135 m s$^{-2}$. Initially the upper layer is 1500 m thick, with a resultant first baroclinic deformation radius of order 33 km at 47°S (similar to that of Wolff et al. 1991). This deformation radius is somewhat larger than in the real Southern Ocean, but this is consistent with the degree of idealization in these simulations. All of the upper-layer PV contours are initially open.

The interpretation of these two-layer simulations as an analog of the Southern Ocean is clearly somewhat troublesome. A model with greater vertical structure would allow the separate resolution of the wind-driven Ekman layer, of other light water masses with a net northward transport (Antarctic Intermediate Water), of the dense unblocked water masses with a net southward transport (including North Atlantic Deep Water and Common Deep Water), and of abyssal, blocked water masses. Such studies with a much richer vertical struc-
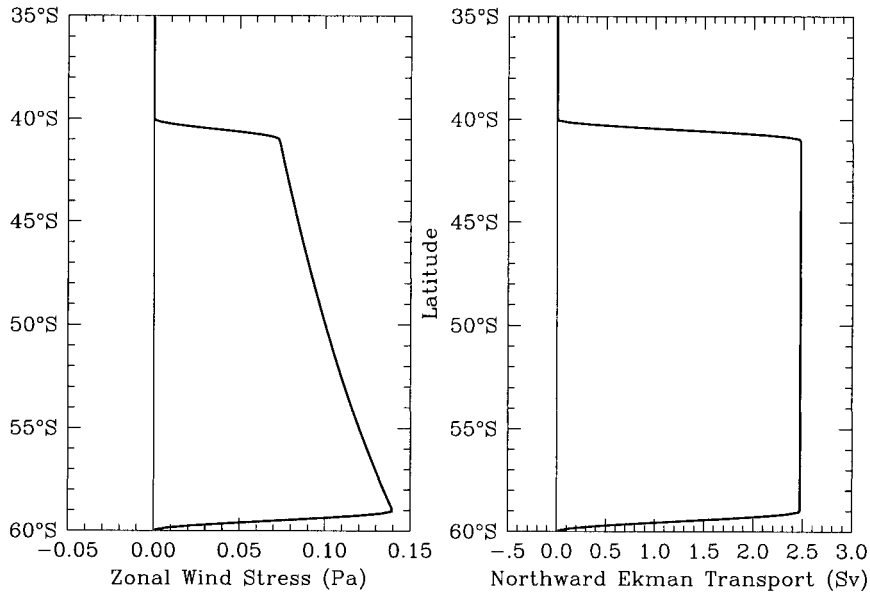
Fig. 3. Plot of the zonally constant zonal wind stress (left) and the zonally integrated northward Ekman transport (right) for the case with the weakest wind stresses. Simulations are also run with wind stresses that are 2, 3, and 4 times as strong. The northward Ekman transport is constant except in regions of diabatic damping.

ture have been done previously (e.g., Webb et al., 1991), and are currently underway at the NOAA Geophysical Fluid Dynamics Laboratory with a horizontal resolution comparable to the simulations shown here. The simplest interpretation of the two-layer simulations here is that the upper layer includes the Ekman layer and the northward moving lighter surface and intermediate water masses; the lower layer includes the denser water masses, both those that are blocked by topography and unblocked ones. With this interpretation, the simple system studied here is qualitatively illustrative of the possible dynamics of the real Antarctic Circumpolar Current.

The horizontal resolution of the simulations, 1/10° latitude by 1/6° longitude, is square at 53°S with a grid spacing of 11 km. With three points to the deformation radius, the eddy dynamics will certainly be affected by the grid resolution, but it is anticipated that the eddy behavior will be qualitatively reasonable. The biharmonic viscosity ($5 \times 10^{10}$ m$^4$ s$^{-1}$) was chosen to limit the viscous control at the eddy length scales.

The simulations are subject to a steady zonal wind forcing. The meridional profile of that wind forcing, shown in Fig. 3, has a uniform zonally integrated northward Ekman transport. All Ekman pumping occurs near the northern or southern boundaries. This choice clearly simplifies the weakly forced balance between the Ekman pumping and diabatic fluxes. It also means that this study is not appropriate for assessing the role of Sverdrup dynamics in the ACC, which has been extensively examined, for example, by Gnanadesikan and Hallberg (2000) and Gent et al. (2001). The strength of the wind

forcing is one of the two parameters that is varied between the simulations.

The other parameter that is varied between the simulations is the timescale with which the internal interface is restored to 1500-m depth within 1° of the southern boundary or within 6° of the northern boundary. The restoration is accomplished by transferring mass across the interface with a diapycnal velocity given by

$$w_{\text{diapycnal}} = (\eta - \eta_{\text{restore}})/T_{\text{restore}} \qquad (2)$$

within the damping regions, where $\eta$ is the interface height, $\eta_{\text{restore}}$ is the unperturbed interface height, and $T_{\text{restore}}$ is the restoring time. The extended northern restoring region acts to fix the stratification at the northern edge of the channel, to mimic the fact that the mean stratification to the north of the Antarctic Circumpolar Current is constrained not to vary rapidly by the bulk of the oceans to the north.

Although interface damping is obviously a very crude representation of the diapycnal fluxes in the real ocean, it does capture some key aspects of the true buoyancy forcing. As pointed out by Warren et al. (1996) one of the major processes that occurs in the Southern Ocean as a result of wind-driven upwelling is that dense Circumpolar Deep Water is freshened and lightened. Thus the interface damping, which acts to increase the depth of the interface in upwelling regions, captures (in a crude sense) the transformation of Circumpolar Deep Water to Antarctic Intermediate Waters and mode waters. Interface damping also captures the sense of the perturbation heat fluxes into the ocean. An upward

anomalous displacement of an isopycnal surface in the real Southern Ocean would tend to be associated with a northward anomalous displacement of the outcrop point of that isopycnal, and hence a generally cold surface temperature anomaly. This colder surface temperature tends to lead to increased net heating of the ocean, which would tend to drive the isopycnal downward. Although the details of the damping are clearly not an accurate depiction of the ocean dynamics, the qualitative sense of this damping is appropriate.

These simulations differ from the quasigeostrophic simulations of Wolff et al. (1991) and McWilliams et al. (1978) primarily in the inclusion of diabatic processes. In many regards, the dynamics elucidated in those exhaustive studies are well representative of the adiabatic limit of the current simulations. It is worth noting, though, that the topography in the present studies is much larger than in the previous studies, so that all potential vorticity (PV) contours are blocked when either the total depth of the fluid or the lower-layer height are considered. By contrast, in most of the runs of Wolff et al. (1991) there are unblocked geostrophic contours in the lower layer, which results in an intense lower-layer zonal current. The blocked PV contours in the current simulations permit substantial, nearly inviscid meridional flows, with PV closure occurring in boundary currents along the northern or southern walls or through direct forcing in the damping regions. By relaxing these assumptions of small amplitude topography and purely adiabatic flow, it is possible to examine flow in a regime where the transient eddies are not necessarily crucial in returning the Ekman transport to the south.

It is still possible, however, that the present configuration overemphasizes the role of transient eddies in determining the structure of the circumpolar current. In particular, the simulations were designed so that the upper-layer height would not go to zero and buoyancy fluxes were limited to occur in the northern and southern sponges. In a multilayer model, if the light water is permitted to outcrop, more of the Ekman flux could be taken up by stationary eddies, as pointed out by Killworth and Nanneh (1994).

## 3. Expected results

The model setup outlined in section 2 assumes that some portion of the Ekman flux can be supplied by a diapycnal flux, which is itself a function of the overall density structure. The diapycnal flux is

$$T_{dia} = A_S \Delta \eta / T_{restore}, \qquad (3)$$

where $A_S$ is the area of the southern sponge and $\Delta \eta$ is the average interface height displacement in the southern sponge. (The northern sponge area and critical interface height displacement could be used instead without changing any results.) As the diapycnal forcing flattens the interface between the two layers, it counteracts the tendency of the Ekman and geostrophic fluxes to make the

upper layer thinner toward the south and the lower layer thinner toward the north. As a result, diapycnal forcing stabilizes the current with respect to baroclinic instability. However, for a given $T_{restore}$ there is a level of diapycnal flux such that $\Delta \eta = \Delta \eta_{crit}$ satisfies the Phillips criterion for baroclinic instability. The ratio of the Ekman flux to this diapycnal flux defines a ratio $R$

$$R = \frac{L_x \tau_x / \rho_o f}{A_S \Delta \eta_{crit} / T_{restore}}, \qquad (4)$$

where $L_x$ is the length of the channel and $\tau_x$ is the eastward wind stress.

The critical interface height displacement is just the value where the lower-layer meridional potential vorticity gradient must be less than or equal to zero somewhere in the channel. This occurs when the lower-layer potential vorticities are equal at the inside edges of the northern and southern restoring zones. For the southern sponge

$$\Delta \eta_{crit} = H_2 \frac{f_S - f_N}{f_N + f_S A_S / A_N}. \qquad (5)$$

Here $H_2$ is the mean lower layer thickness, and $f_N$ and $f_S$ are the Coriolis parameters at the edges of the northern and southern sponges; $A_N$ is the area of the northern sponge. This expression assumes that the magnitudes of the interface displacements in the two sponges are inversely proportional to the areas of the two sponges so that there is zero net tendency in the volume of the lower layer. It also assumes that the interface displacement is constant within each sponge, which Fig. 11 will later show not to be strictly true.

The lower-layer thickness is the pertinent one, since with an eastward wind stress, it is the lower-layer potential vorticity gradient that opposes the planetary vorticity gradient, satisfying a necessary condition for baroclinic instability in the Phillips model (Pedlosky 1987). It is not completely clear that this is the only parameter of importance since the presence of topography means that the lower-layer potential vorticity gradient is not aligned with the upper-layer potential vorticity gradient, allowing for localized baroclinic instability to develop over the topography. By choosing $H_2$ to be the value in the deep portion of the domain, 2500 m, $R = 1$ essentially defines an upper bound at which baroclinic instability can develop anywhere along the channel. With the parameters in these simulations, the lower layer is initially half as thick over the top of the ridge as it is at depth, so baroclinic instability might be expected in the vicinity of the ridge for $R > 0.5$, even ignoring any destabilizing effects of the topography or the horizontal velocity shears.

A total of 15 simulations were performed for this study. The values of wind stress and damping used are indicated in Table 1, with abbreviations for each case and the value of $R$ also given. The case that would be

TABLE 1. Summary of the runs used in this study. The wind stress at 50°S and the restoring (in years) are used to denote individual runs. Abbreviations for the runs are shown by the letters. Values of $R$ are shown in parentheses.

| Restoring time (yr) | Wind stress at 50°S (Pa) | | | |
|---|---|---|---|---|
| | 1 | 2 | 3 | 4 |
| 1/2 | W1D05 (0.2) | W2D05 (0.4) | W3D05 (0.6) | W4D05 (0.8) |
| 1 | W1D1 (0.4) | W2D1 (0.8) | — | W4D1 (1.6) |
| 2 | W1D2 (0.8) | W2D2 (1.6) | — | W4D2 (3.2) |
| 4 | W1D4 (1.6) | W2D4 (3.2) | — | W4D4 (6.5) |
| 8 | W1D8 (3.2) | W2D8 (6.5) | — | — |

W4D8 could not be run with the same value of the biharmonic viscosity as the other simulations.

When $R$ is much less than 1, the diapycnal mass fluxes alone can provide the source and sink for the Ekman flux without any baroclinic instability developing. In this case, the southward net mass flux in the abyssal layer exactly balances the northward Ekman flux in the upper layer, as depicted in Fig. 1a. If the Ekman flux, diapycnal, and eddy fluxes are defined as $T_{\text{Ekman}}$, $T_{\text{dia}}$, and $T_{\text{eddy}}$, respectively, in this limit

$$T_{\text{Ekman}} = -T_{\text{dia}} \quad \text{and} \quad |T_{\text{dia}}| \gg |T_{\text{eddy}}|. \qquad (6)$$

This limit is similar in some regards to the circulation that develops in coarse-resolution ocean GCM simulations without an eddy parameterization of the sort proposed by Gent et al. (1995). The large diapycnal fluxes to the south of the ACC are provided by mixing in the surface layer, even if the explicit diffusion below this layer is modest. The diapycnal fluxes to the north of the ACC are provided by deep-water formation in the North Atlantic. It is in this limit that the direct connection between the Southern Ocean winds and the Atlantic overturning described by Toggweiler and Samuels (1993, 1995, 1998) should be most prominent.

When $R$ is greater than 1, baroclinic instability develops, and some of the compensating southward mass flux can occur in the upper layer. When $R$ becomes very large, it is anticipated that eddy saturation will limit the magnitude of the interface slope, and it may be difficult for the slope to greatly exceed the value that gives zero or negative meridional potential vorticity gradients everywhere in the lower layer (Marshall et al. 1993). In the limit of large $R$, the eddy mass fluxes will greatly exceed the diapycnal mass fluxes.

In the limit where $R$ is large, changes in the Ekman flux must be compensated by changes in the eddy fluxes. If the wind increases, the eddy energy must increase, with one of two possible effects. The first is that the transient eddy fluxes of mass could increase. Insofar as such fluxes can be parameterized in terms of the diffusion of the upper-layer thickness (Gent and McWilliams 1990; Gent et al. 1995; Visbeck et al. 1997; Griffies 1998), this would result in a diffusion coefficient that was dependent on wind stress (or perhaps very strongly dependent on the departure of the slope from some critical value of stability). This is the situation portrayed in Fig. 1c. One key assumption here is that

the eddies act to reduce the total energy. However, it is also possible that the eddies could act to homogenize potential vorticity in the lower layer, moving the lower layer toward a situation more similar to that shown in Fig. 1b, where stationary eddies play a dominant role.

The marginal cases, when $R$ is slightly larger than 1, are in many ways the most interesting. Eddies and buoyancy fluxes both play important roles in maintaining the mean isopycnal slopes in this range of parameter space. But the marginal importance of the two fluxes may differ significantly from their mean importance. For example, changes in the wind stress might be compensated almost entirely by changes in the eddy intensity, even though the eddy and diapycnal fluxes are of comparable magnitude. In this limit then

$$T_{\text{Ekman}} = -(T_{\text{dia}} + T_{\text{eddy}}), \qquad (7)$$

but it may well be that

$$|dT_{\text{eddy}}/dT_{\text{Ekman}}| \gg |dT_{\text{dia}}/dT_{\text{Ekman}}|, \qquad (8)$$

even though $T_{\text{dia}} \approx T_{\text{eddy}}$. Both the spatial extent of the baroclinic instability (i.e., the region where $H_2$ is small enough for reversed meridional PV gradients to occur) and the eddy growth rates may be strong functions of the supercriticality of the isopycnal slopes. Similarly, the relative sensitivity of the standing and transient eddies may differ markedly.

The marginal case also is most likely to pertain to the ACC. A typical estimate of the maximum northward Ekman transport in the unblocked latitudes of the ACC is 30–45 Sv (Trenberth et al. 1989; Kalnay et al. 1996), while the formation rate of North Atlantic Deep Water (which might be roughly equated with $T_{\text{dia}}$) is around 16–18 Sv with estimates of Antarctic Intermediate Water formation ranging from 14 to 26 Sv (Schmitz 1995; MacDonald 1998; de las Heras and Schlitzer 1999). It is thus reasonable to anticipate that $T_{\text{dia}}$ and $T_{\text{eddy}}$ will be of comparable magnitudes.

It should be emphasized at this point that the breakdown into stationary and transient eddies depends on the coordinate system employed. This can be shown as follows. The momentum equation can be written

$$\frac{\partial \mathbf{u}}{\partial t} + (f + \zeta)\mathbf{k} \times \mathbf{u} = -\nabla B + \mathbf{F}, \qquad (9)$$

where bold symbols are vectors. In this equation $f$ is the planetary and $\zeta$ the vertical component of relative
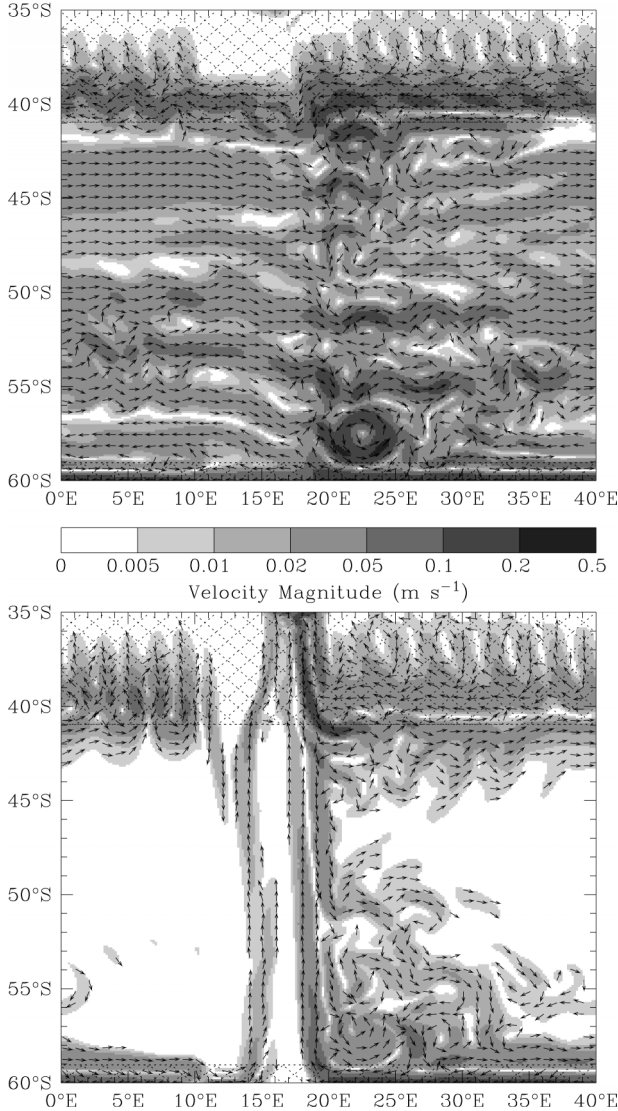
FIG. 4. Velocities at day 14 000 of the most weakly forced and strongly damped case, W1D05, in the upper (top) and lower (bottom) layers: $R = 0.2$ for W1D05. The magnitude of the velocities is indicated by the shading, while directions are shown by the arrows where the velocities are sufficiently large.

vorticity, $\mathbf{k}$ the vertical normal vector, $B$ the Bernoulli function, and $\mathbf{F}$ frictional forcing. If a time mean is taken,

$$\mathbf{k} \times ((f + \overline{\zeta})\overline{\mathbf{u}} + \overline{\zeta'\mathbf{u}'}) = -\nabla\overline{B} + \overline{\mathbf{F}}. \quad (10)$$

Equation (10) can be simplified by taking the dot product with $\overline{h}\mathbf{t}$, where $\mathbf{t}$ is the unit vector tangential to some contour $C$ (and directed eastward for a zonally reentrant contour or clockwise around a closed contour) and $\overline{h}$ is the time average layer thickness:

$$\overline{\zeta}_a \overline{v}_C \overline{h} + \overline{h}\,\overline{v_C'\zeta'} + \overline{h}\mathbf{t} \cdot \nabla\overline{B} - \overline{h}\mathbf{t} \cdot \overline{\mathbf{F}} = 0. \quad (11)$$

This expression uses definitions for the absolute vortic-

ity $\overline{\zeta}_a \equiv f + \overline{\zeta}$ and the velocities along and across the contour, $u_C \equiv \mathbf{t} \cdot \mathbf{u}$ and $v_C \equiv (\mathbf{k} \times \mathbf{t}) \cdot \mathbf{u}$.

If the system is in steady state, the continuity equation can be integrated over the region bounded by the contour to give

$$\oint_C \overline{v}_C\overline{h}\,ds = M_s - \oint_C \overline{v_C'h'}\,ds, \quad (12)$$

where $M_s$ is the mass flux into the layer to the south of the contour or inside the contour. Defining $\tilde{Q} = \overline{\zeta}_a/\overline{h}$ and assuming that this quantity is nowhere equal to zero, (11) and (12) can be combined to give

$$M_s = \oint_C \left( \overline{v_C'h'} - \frac{1}{\tilde{Q}}\overline{\zeta'v_C'} - \frac{1}{\tilde{Q}}\mathbf{t} \cdot \nabla\overline{B} + \frac{1}{\tilde{Q}}\mathbf{t} \cdot \overline{\mathbf{F}} \right) ds. \quad (13)$$

In the small Rossby number limit this reduces to

diapycnal flux = transient eddy mass flux

+ Reynolds momentum flux

+ stationary eddy flux

+ Ekman flux.          (14)

The exact term balance can depend on the choice of $C$. As will be shown more clearly later in this paper, when a zonal contour is chosen, the stationary (geostrophic) eddy fluxes will dominate the balance. However, when a contour of constant Bernoulli function is chosen $\mathbf{t} \cdot \nabla\overline{B} = 0$ so that the stationary geostrophic eddy flux normal to the contour vanishes. In general, the horizontal Reynolds momentum flux term is small (see, e.g., Johnson and Bryden 1989; MacCready and Rhines, 2001; Tansley and Marshall, 2001) so that along a contour of constant Bernoulli function the transient eddy term would be expected to dominate. Gille (1997) looked for this balance to hold in the Semtner–Chervin general circulation model but concluded that subgrid-scale friction was, in fact, dominant. However, Tansley and Marshall (2001) do find this balance in a set of runs similar to ours but without buoyancy forcing.

## 4. Results from simulations

The simulations presented in this paper cover a 32-fold range of $R$, from W1D05 (with $R = 0.2$) to W4D4 and W2D8 (with $R = 6.5$). As expected, the most weakly forced and strongly damped cases exhibit a largely diapycnal overturning circulation and very weak eddy activity. Meridional eddy fluxes figure prominently in the balance in the most strongly forced and weakly damped cases. In these large $R$ cases the strength of the zonal current is largely insensitive to changes in forcing, although the path of the current (and the stationary eddy flux across a zonal contour) do exhibit large changes.

The most weakly forced and strongly damped case, W1D05, is depicted in Fig. 4. The nondimensional parameter $R = 0.2$ for this run, so it would be expected

that diapycnal fluxes would dominate the mass balance. The upper-layer flow is essentially zonal with standing Rossby waves occurring in the lee of the topography. (These waves are longer than would be expected based on the mean zonal velocities for barotropic Rossby waves but shorter than for flat-bottom baroclinic mode waves.) There are localized regions of baroclinic instability to the east of the southern and northern parts of the ridge associated with reversals in the lower-layer meridional potential vorticity gradient near the edges of the damping. These eddies are not significant in the overall momentum or mass balances, although they are probably significant in the formation of the zonal jets that appear farther downstream of the ridge. The upper-layer meridional mass fluxes are due almost entirely to the broadly distributed Ekman transport. The lower-layer flow is largely confined to the flanks of the ridge and the edges of the damping. The flow consists of opposing currents with the deeper flow carrying the southward net meridional transport in the lower layer. Much of the lower-layer flow (including the sense of the meridional flow on the eastern flank of the ridge) can be described in terms of diabatically forced topographically modified beta plumes, as in Hallberg and Rhines (1996). The zonal mean overturning flow in this case is well characterized by the diapycnal overturning circulation, described qualitatively in Fig. 1a.

Eddy fluxes are quite significant in the most weakly damped of the most strongly forced cases, W4D4. A rich field of equivalent barotropic eddies is evident downstream of the ridge in Fig. 5. The upper-layer mean flow is strongly, persistently deflected northward over the ridge. The net (stationary eddy) southward transport due to this deflection (i.e., the zonal integral of the meridional velocity times the layer thickness) largely balances the northward Ekman transport. Associated with this deflection of the mean current, interfacial form stress over the ridge balances eastward momentum imparted to the upper layer by the wind (as argued by, e.g., Marshall et al. 1993; Gille 1997). The time-mean flow consists of a series of zonal jets, but these are masked to the east of the ridge by the strong eddy field. There is a strong asymmetry about the ridge in the eddy field: the flow on the western flank of the ridge is quite steady, while the eddy field dominates the flow to the east of the ridge. The zonal mean balances in this case are well characterized by the standing eddy balance, depicted in Fig. 1b, with some contribution from transient eddies.

The dependence of the zonal current transport, eddy kinetic energy, and overturning circulation on $R$ generally conforms to expectations. The zonal current transport (Fig. 6a) increases nearly linearly with increasing $R$ for $R < 1$, but is relatively insensitive to $R$ for $R > 1$. Eddy saturation theories would suggest an abrupt transition between these two limits (Marshall et al. 1993), but the transition in these simulations is more gradual than such theories might suggest. Baroclinic
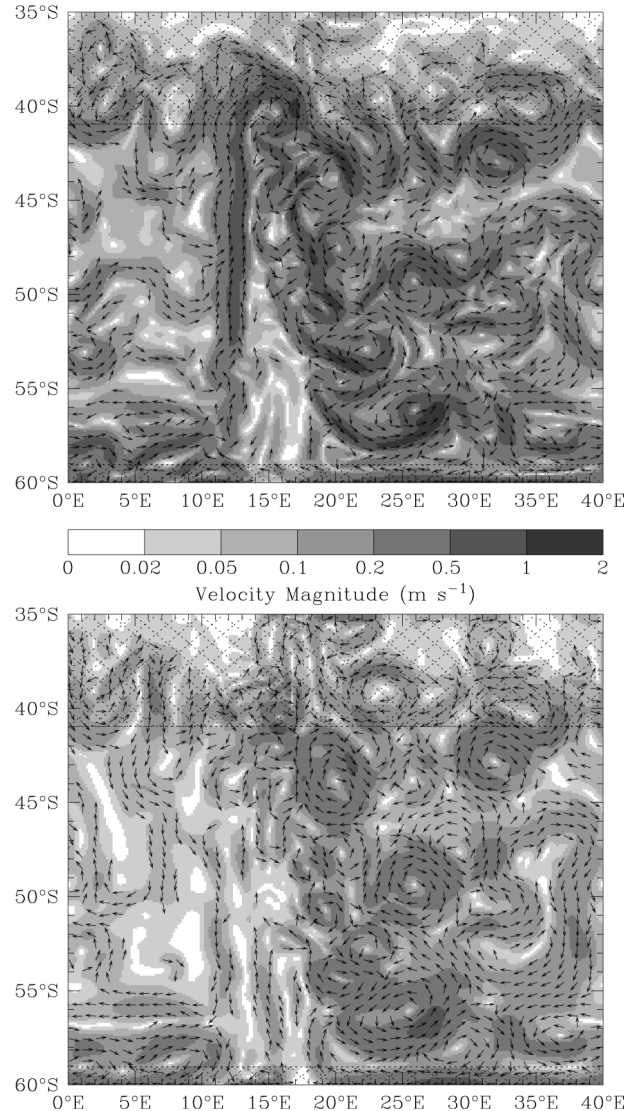


FIG. 5. Velocities at day 14 000 of the most strongly forced and weakly damped case, W4D4, in the upper (top) and lower (bottom) layers: $R = 6.5$ for W4D4. The magnitude of the velocities is indicated by the shading, while directions are shown by the arrows where the velocities are sufficiently large. Note that the grayscale is 4 times larger than in Fig. 4, corresponding to a fourfold increase in the Ekman transport.

instability occurs only in a very limited region near the ridge for small $R$, but the spatial extent of the unstable flow increases with increasing $R$. If the entire channel became baroclinically unstable at the same value of $R$, saturation theories would be more likely to apply. The eddy kinetic energy (Fig. 6b) generally increases with $R$. There is a certain amount of scatter in the points however, so runs with identical values of $R$ have different values of EKE. Given two runs with the same $R$, the one with stronger winds always has a higher level of EKE. No such consistent signal is found for zonal current transport.
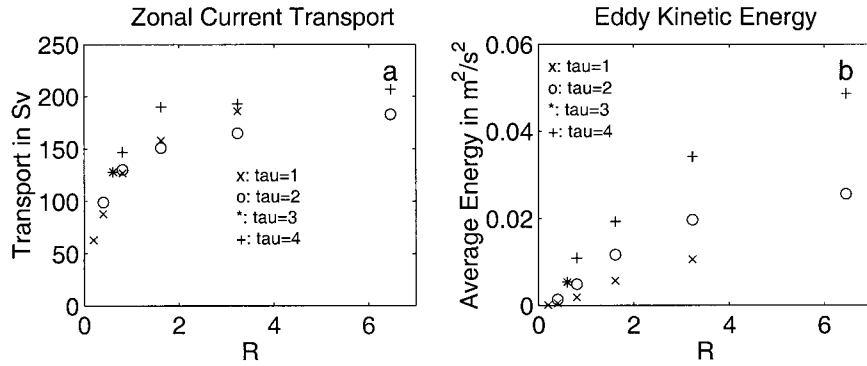
FIG. 6. Relationship between the zonal current transport and EKE and $R$, the nondimensional ratio of Ekman transport to diapycnal fluxes at the marginal shear for baroclinic instability. (a) Zonal current transport showing a strong dependence on $R$ for small values of $R$, weak dependence on $R$ for large values. (b) EKE in the center of the channel. Note that while there is a general increase as $R$ increases, there is still quite a bit of variability for a given value of $R$.

The ensemble of model runs can also be used to examine how the Ekman flux across zonal contours is supplied as a function of $R$ (Fig. 7). For $R < 1$, baroclinic instability plays a minor role and the Ekman flux is supplied by diapycnal fluxes, as can be seen in Fig. 7a. As $R$ increases past 1, the diapycnal fluxes are less and less efficient, and the ratio of diapycnal flux (which is limited by the slope of baroclinic instability) to Ekman flux is expected to scale as $1/R$. This is approximately true, but the transition is not as sharp as the simple theory would suggest, since transient eddies and stationary eddies begin to play a role at relatively low values of $R$. The ratios of the transient and stationary eddy fluxes to the Ekman flux have a more complicated behavior (Figs. 7b and 7c). Both generally increase as $R$ increases, but there is strong dependence on wind stress as well. The actual transient eddy fluxes are relatively invariant at a constant value of $R$. By contrast, the diapycnal fluxes are nearly proportional to the wind stresses at constant $R$ (essentially by the definition of $R$), and the stationary flux is disproportionately sensitive

to the strength of the forcing. Given a constant value of $R$, higher values of wind stress have a lower transient eddy fraction and a higher stationary eddy fraction.

That the breakdown between transient and stationary eddy flux depends on wind stress as well as $R$ can be understood by focusing on the cases with moderate values of $R$, in particular W4D2 and W8D1, both of which have $R = 3.2$. The mean kinetic energy and streamfunction for the upper layer of these two cases is shown in Fig. 8. The upper-layer mean flow in both cases consists largely of eastward jets over the flat abyss and a strong meridional deflection over the ridge. The number of jets increases downstream of the ridge in both cases (and the spacing between them decreases), and there are more jets in the more weakly forced case. The jet spacing in both cases is generally consistent with the usual $\sqrt{U_{eddy}}/\beta$ (where $\beta$ is the north–south gradient of the Coriolis parameter) scaling of jets emerging from geostrophic turbulence (Rhines 1977). The meridional deflection of the mean current is much larger in the more strongly forced case. In fact, it extends essentially from
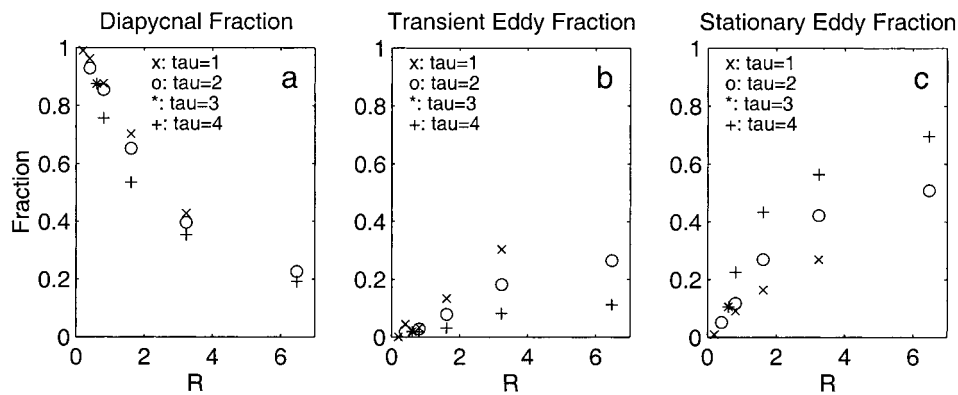


FIG. 7. Relationship between the supply of Ekman flux and $R$, averaged along zonal contours. (a) Diapycnal flux. When $R$ is small, diapycnal fluxes dominate. As $R$ increases, eddy fluxes dominate. (b) Transient eddy flux. Although there is an increase with $R$, there is clear dependence on other parameters. (c) Stationary eddy flux. Note that this comes to dominate the transient eddy flux at large $R$.
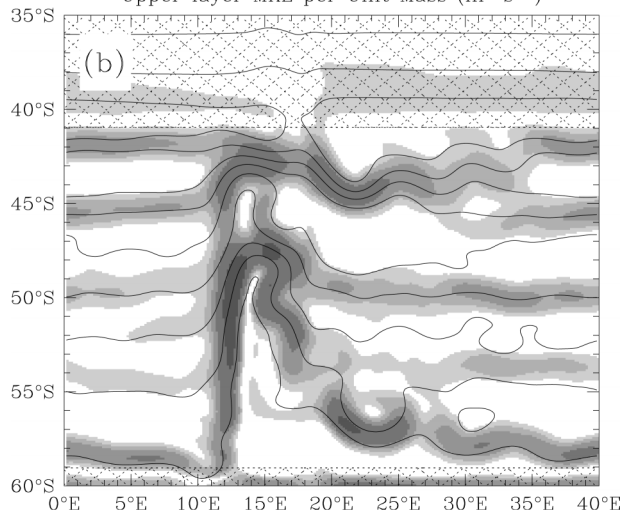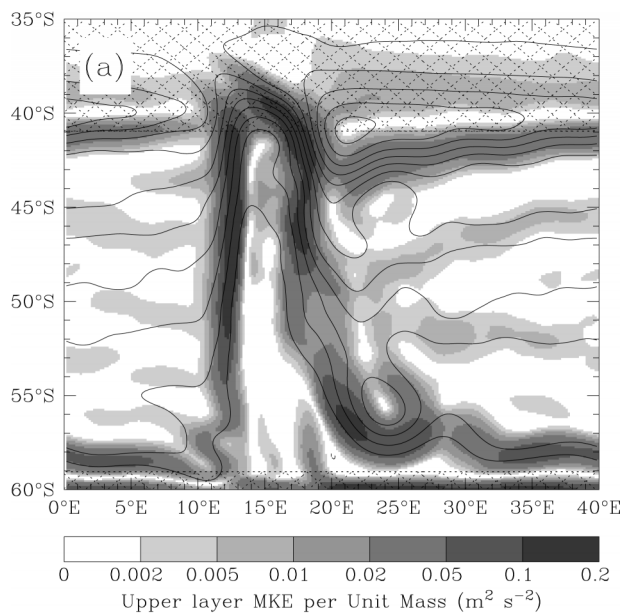
FIG. 8. Mean kinetic energy per unit mass ($\frac{1}{2}\overline{\mathbf{u}} \cdot \overline{\mathbf{u}}$) (shaded) and mean streamlines (contours) in the upper layer averaged over 2500 days in cases (a) W4D2 and (b) W1D8. The interface damping regions are hatched. The contour interval for the streamlines is 20 Sv. Both runs have $R = 3.2$, but the wind forcing and damping in W4D2 are 4 times stronger than in W1D8.

FIG. 9. Time-mean EKE per unit mass ($\frac{1}{2}\overline{h\mathbf{u} \cdot \mathbf{u}}/\overline{h} - \frac{1}{2}\overline{\mathbf{u}} \cdot \overline{\mathbf{u}}$) in the upper layer averaged over 2500 days in cases (a) W4D2 and (b) W1D8. As in Fig. 8, the damping regions are hatched and time-mean streamlines are overlaid with contour interval 20 Sv.

the Ekman convergence region in the north to the Ekman divergence region in the south (which are collocated with the diabatic damping regions). It is not surprising, then, that meridional advection by this mean current balances over half of the Ekman transport in case W4D2. In the more weakly forced case, W1D8, the mean current is much more nearly zonal and accomplishes relatively little net meridional transport.

In both cases there is a vigorous transient eddy field centered downstream of the topography (Fig. 9). Gille and Kelly (1996) find a similar picture in the Southern Ocean using altimeter data. Just downstream of the topography, the flows tend to tilt against the mean shear,
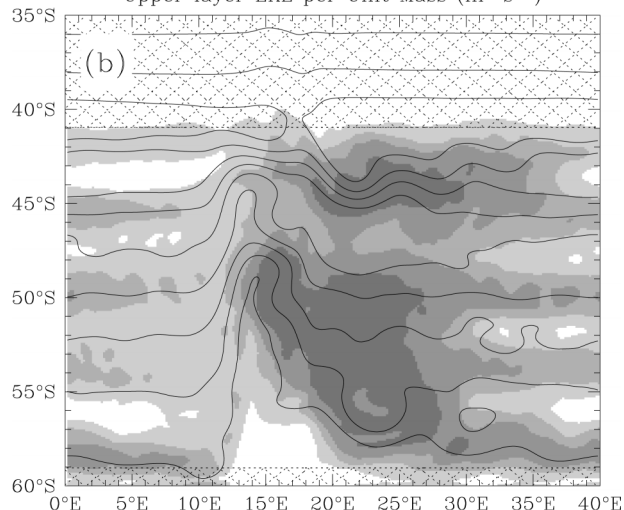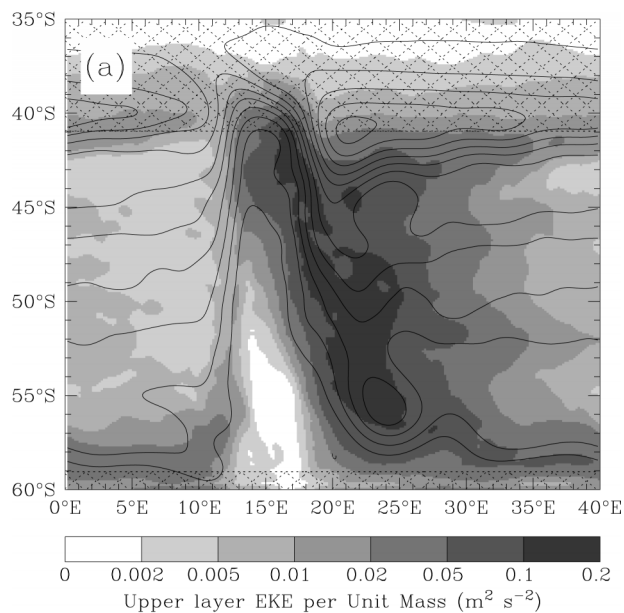
as would be expected of growing instabilities, while farther to the east the motions are better described as equivalent barotropic. The eddy kinetic energies are roughly four times larger in case W4D2 than in W1D8, commensurate with the fourfold stronger wind stress. The areal and temporal mean upper-layer zonal velocities differ by only 4% between these two cases, so the energy imparted by the winds scales linearly with the wind stress, and it is perhaps not surprising that the EKE should also scale linearly with the wind stress. In both cases, the difference in eddy intensity upstream and downstream of the ridge is particularly striking, given that the velocity shears are roughly symmetric about the ridge.

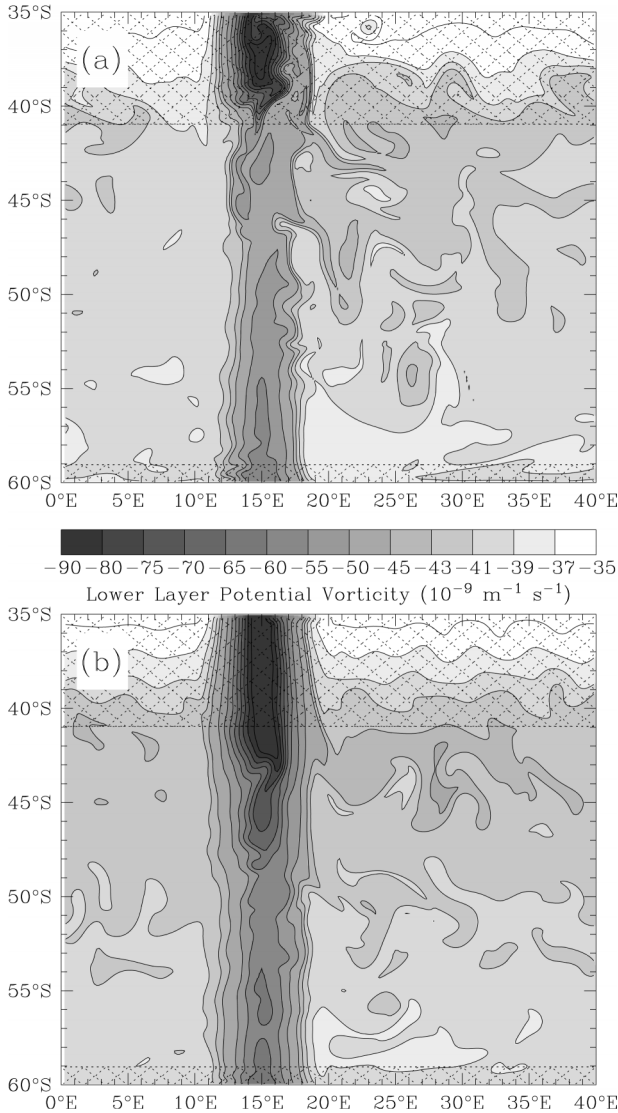Higher values of EKE for constant $R$ are associated

FIG. 10. Lower-layer potential vorticity at day 14 000 in cases (a) W4D2 and (b) W1D8. Both simulations have $R = 3.2$. Away from the topography the potential vorticity is fairly homogenous with weak gradients in the opposite direction to the planetary vorticity gradient. In the case with stronger forcing, W4D2, the potential vorticity is much more nearly homogenized between the ridge and the abyss than in the case with weaker forcing.

FIG. 11. Time-mean interface heights along 45°S (top) and along 30°E (bottom) in three runs with $R = 3.2$. The free surface height has been exaggerated by a factor of 360 in this figure. The reduced gravity across the interior interface is 720 times smaller than that across the free surface, so in this figure slopes in the free surface have twice the effect on pressure gradients of comparable magnitude internal interface displacements. Over the ridge the internal interface is progressively more strongly deflected with increasing forcing, but downstream of the ridge the differences in the meridional profiles are very similar between the three cases.

with a lower-layer potential vorticity field that is more homogeneous over the topography. This can be seen in Fig. 10, which compares the lower-layer PV fields for W1D8 and W4D2. In both cases there is essentially no PV gradient in the interior of the fluid. Such homogenization of the interior PV field is consistent with the idea that baroclinic instability sets in when the sign of the lower-layer potential vorticity gradient becomes opposite to that in the upper layer, and then proceeds to drive the lower layer toward vanishing PV gradients (Rhines and Young 1982). However, there are significant differences between the lower-layer PV over the ridge
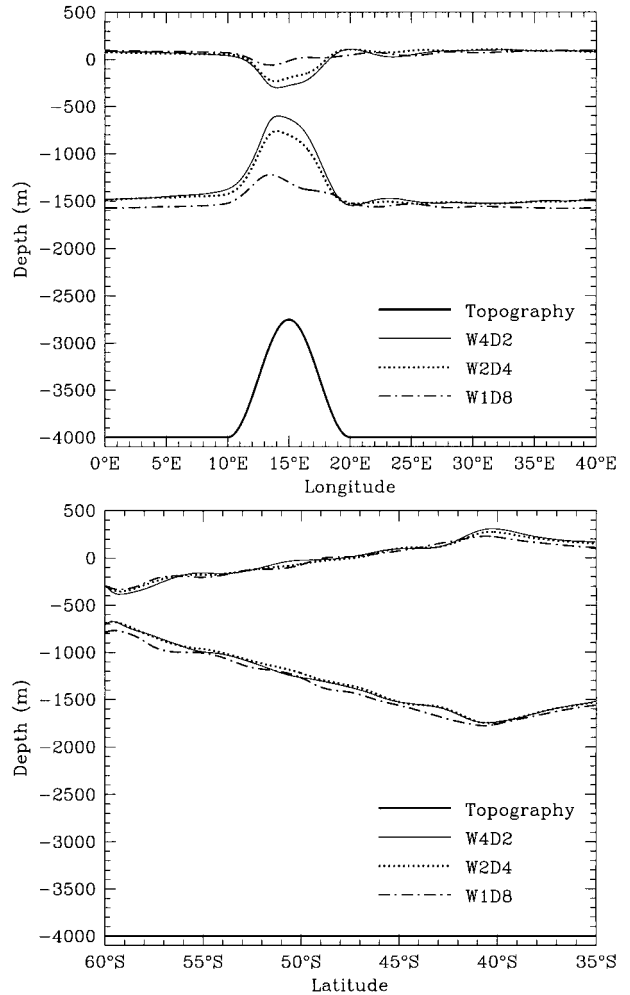
and over the flat abyss, with a noticeably larger contrast between the PV of interior and ridge in the lower EKE case (W1D8).

The homogenization of lower-layer potential vorticity over the ridge is associated with a change in the height of the internal interface. This is clearly seen in Fig. 11a, which shows the time-mean surface and interface height averaged along a zonal contour in the middle of the basin for the three cases with $R = 3.2$. As the wind and damping increase, the interface deflection over the ridge becomes larger and the picture increasingly resembles Fig. 1b. By contrast, a time-mean meridional interface height transect to the east of the ridge (Fig. 11b) is essentially identical for the three cases.
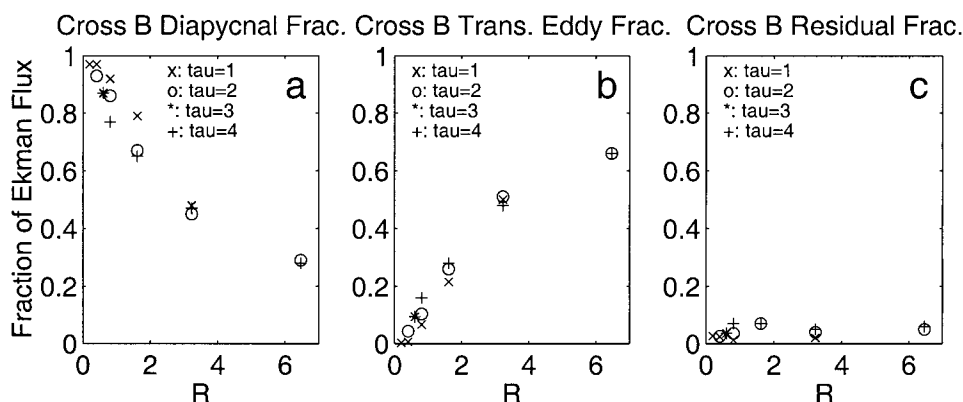
FIG. 12. Ekman supply across contours of constant Bernoulli function rather than zonal contours as in Fig. 7. (a) Fraction supplied by diapycnal flux (numbers are slightly different from Fig. 7 since some contours enter the damping regions where the Ekman flux is smaller). (b) Transient eddy flux. (c) Residual steady ageostrophic fluxes.

Changes in path of the current are responsible for masking the effect of the transient eddies on the supply of the Ekman flux. This can be seen when the mass balance is computed across lines of constant Bernoulli function (which follow the streamfunction and interface height relatively closely) instead of lines of constant latitude. As can be seen in Fig. 12, when the integral is performed in these coordinates, the dominant balance is between Ekman, diapycnal, and transient eddy fluxes, with residual ageostrophic fluxes playing a relatively minor role. These residual ageostrophic fluxes appear in (14) as the Reynolds momentum flux plus the part of the Ekman flux due to the biharmonic viscosity and interior vertical viscosity. The values plotted in Fig. 12 are an average over a range of largely unforced Bernoulli function contours, but it is perhaps not surprising that these results are insensitive to which Bernoulli function contours are used. At high values of $R$, the Ekman flux is largely compensated adiabatically by transient eddies, while at low values of $R$ it is primarily supplied by diapycnal forcing. Essentially, as the winds become stronger, the eddy field increases, the current is deflected more over the ridge, and more of the transient eddy flux is in the zonal direction rather than in the meridional direction (Fig. 13). This balance in eddy-rich cases, between transient eddy fluxes across mean streamlines and Ekman transport, is essentially in agreement with the arguments of Marshall et al. (1993), Ivchenko et al. (1996), and Gille (1997), and has also been found in the idealized numerical simulations of Tansley and Marshall (2001) and MacCready and Rhines (2001).

However, the changes in the fluxes are by no means unambiguously dominated by transient eddies when *fixed* control contours are used. Qualitatively, the largest changes between the various simulations with the same values of $R$ are in the path of the current. Mean streamlines can significantly shift their locations in response to changes in forcing, and there is not a meaningful choice of control contours that will (by construction) largely eliminate either the stationary or transient eddy fluxes from the changes in the balance. Theories that rely upon fixed locations of streamlines, or which ignore stationary eddy fluxes (such as the suggestion that the current strength is proportional to wind stress along key geostrophic contours or other paths), suffer from this assumption.

A key result of these runs is to show that topography controls not only the stationary but also the transient eddy fields and associated fluxes. This raises a number
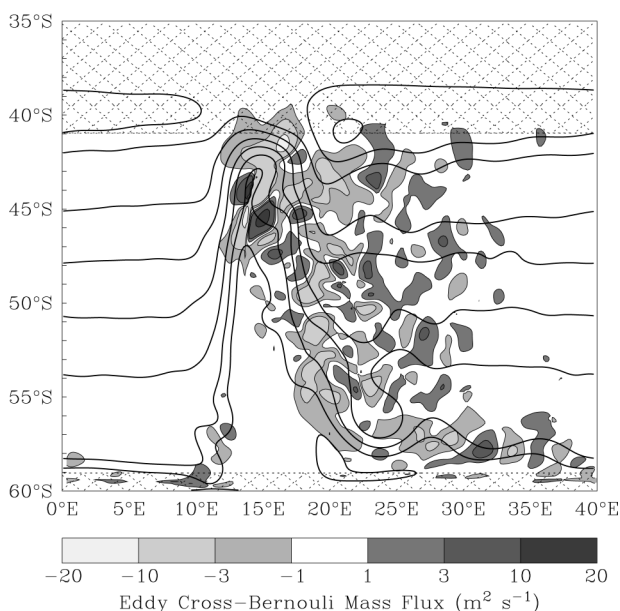


FIG. 13. Cross-Bernoulli-function transient eddy mass flux in the upper layer for case W2D4, with overlaid time-mean upper-layer Bernoulli function contours. Negative fluxes are from high Bernoulli function to low, which is generally southward. Note that much of the flux occurs in regions where the Bernoulli function contours are sloping from north to south implying a flux from east to west.
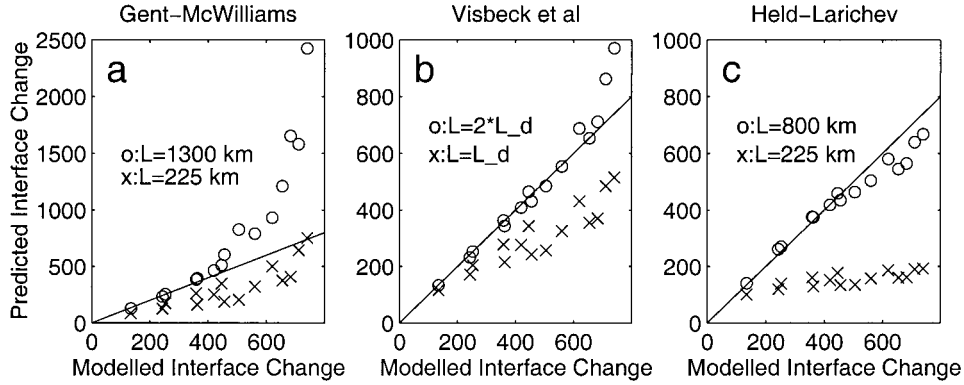
FIG. 14. Interface height displacements predicted by three recent parameterizations of transient eddy fluxes. The straight lines have a slope of 1 and indicate when the simulations agree with the predictions of the theories. (a) Gent and McWilliams (1990) with two values for the spatial scale $l$ over which the upper-layer height changes [from Eq. (17)]. (b) Visbeck et al. (1997) using two values for the ratio between the turbulence scale $l_d$ and $l$. Values are found by solving (19). (c) Held and Larichev (1996) using two values for $l$. Values are found by solving (20).

of questions about how well the model setup represents the real circumpolar current system. In particular, does the small domain size result in an overestimate in the importance of topography (since in the real ocean it seems likely that there are only three or four major topographic features that are associated with transient eddy generation)? In order to evaluate this question, a single simulation was made with the same single ridge but with a longitudinal extent of 120° rather than 40°. Somewhat surprisingly, this run showed even more concentration of the eddy activity and cross-Bernoulli mass fluxes immediately downstream of topography than in the smaller domain.

It is interesting to compare the results from the eddy resolving runs with calculations of how the interface height might be expected to scale if a bulk parameterization of the eddy fluxes based on local density slopes is used. If the assumption is made that the transient eddy mass flux can be parameterized in terms of a diffusion of upper-layer thickness,

$$T_{\text{eddy}} = A_I \boldsymbol{\nabla} H = A_I \Delta \eta / l, \qquad (15)$$

where $\Delta \eta$, as before, is the interface displacement in the southern sponge, $A_I$ is a diffusion coefficient, $l$ is a characteristic length scale for changes in interface height.

If the constant-coefficient parameterization of Gent and McWilliams (1990) is used for $A_I$, then setting the Ekman flux equal to the sum of the transient eddy flux and the diapycnal flux yields

$$\frac{\tau_x}{\rho f} = A_I \frac{\Delta \eta}{l} + \frac{\Delta \eta l_s}{T_{\text{restore}}}, \qquad (16)$$

where $l_s$ is the width of the southern sponge. It can be seen that for this parameterization,

$$\Delta \eta = \frac{\tau_x}{\rho f(A_I/l + l_s/T_{\text{restore}})} \qquad (17)$$

so that there is a linear dependence on wind stress. The effect of adding the eddy parameterization in this case is to reduce the slope of the dependence on wind stress, but not to cause it to asymptote to some constant value. As seen in Fig. 14a, when $A_I = 1000$ m$^2$ s$^{-1}$ (a value consistent with that seen in subtropical gyres and consistent with eddy-resolving runs of Lee et al. 1997) and $l = 1300$ km (corresponding to the width of the channel) are used, the Gent and McWilliams (1990) parameterization fails to capture the effect of transient eddies in returning the Ekman flux to the south, overestimating the height change at high winds. By contrast, when $l = 225$ km (corresponding to the actual width of the baroclinic zone in the high $R$ cases), the height perturbation is underestimated at low wind stresses.

The scheme of Visbeck et al. (1997) is somewhat better at reproducing these simulations. In this scheme

$$A_I = \frac{\alpha l^2 f}{\text{Ri}^{1/2}} = \alpha N l_d^2 |\boldsymbol{\nabla} H_1|, \qquad (18)$$

where $l_d$ is a length scale for the turbulence, $H_1$ is the upper-layer thickness, $\alpha$ a nondimensional constant, and

$$f/\text{Ri}^{1/2} = \frac{f}{N}\frac{\partial U}{\partial z} \approx N|\boldsymbol{\nabla} H_1|$$

is the Eady growth rate. In this case

$$\frac{\tau_x}{\rho f} = \alpha N \frac{l_d^2}{l^2}(\Delta \eta)^2 + \frac{\Delta \eta l_s}{T_{\text{restore}}}, \qquad (19)$$

yielding a quadratic equation that can easily be solved for $\Delta \eta$. With this parameterization, when the wind stress is very large or the restoring time very long, the height anomaly scales as the square root of wind stress. The key parameters are the ratio $l_d/l$, which Visbeck et al. (1997) argue should be order 1, and $\alpha$, which they find to be about 0.015 for a wide range of examples of baroclinic instability in homogeneous environments. Using
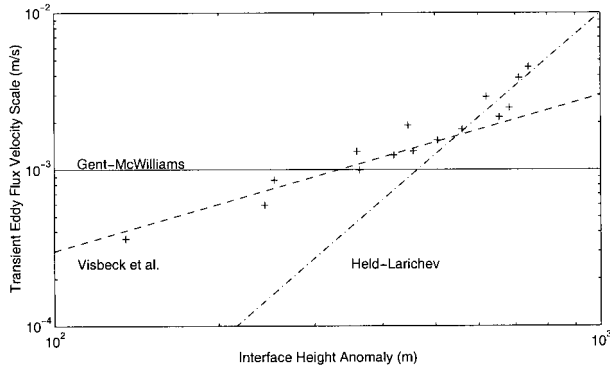
FIG. 15. Scaling of eddy scaling velocity $v_e = A_I/l$ vs interface height anomaly $\Delta\eta$. Assuming constant values for $l$, this corresponds to seeking a power law dependence for $A_I$ on $\Delta\eta$. Note that the Gent–McWilliams parameterization performs poorly here, while the Visbeck et al. parameterization performs better except near saturation. At large values of $\Delta\eta$ the Held–Larichev parameterization is superior.
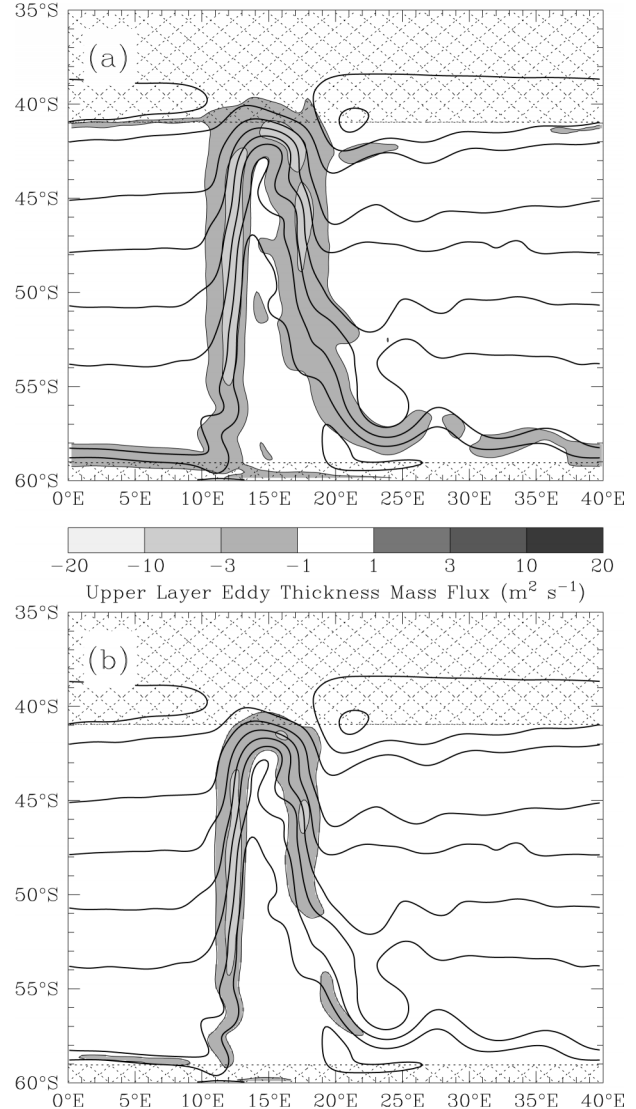


FIG. 16. Cross-mean-Bernoulli-function mass fluxes that would be generated by the parameterization of (a) Gent et al. (1995) and (b) Visbeck et al. (1997). These fluxes are based on the mean layer thicknesses from case W2D4 (the same case as in Fig. 13), and do not include the effect that these parameterizations would have on the flow. The magnitudes are arbitrary, and are fit to the respective constant coefficients.

these parameter settings does not give good agreement for the runs presented here (Fig. 14b). However, setting $l_d/l = 1/2$ does give a good fit to the model results at all but the highest wind stresses, where the Visbeck et al. (1997) parameterization continues to allow for an increase in the height anomaly. Again we see that the parameterization works well when the large-scale density structure is considered but breaks down when the small-scale gradients over topography are used.

Finally, the scheme of Held and Larichev (1996) parameterizes the diffusion coefficient as $A_I = (C/\beta^2)(f/\mathrm{Ri}^{1/2})^{-3}$ where $(f/\mathrm{Ri}^{1/2})$ is (as before) the Eady growth rate, and $C$ is a nondimensional constant of order 1 ($C$ is set to 1 in calculating the field shown in Fig. 14c). Then

$$\frac{\tau_x}{\rho f} = \frac{CN^3}{\beta^2 l^4}(\Delta\eta)^4 + \frac{\Delta\eta l_s}{T_{\mathrm{restore}}}. \quad (20)$$

The interface displacement has an even weaker dependence on wind stress than the other parameterizations when $T_{\mathrm{restore}}$ is large (Fig. 14c). This parameterization gives the best fit to the model, but only when a large value is used for $l$. When a small value is used, it produces by far the worst result.

An alternative way of looking at this problem is to look at the scaling of $v_e = A_I/l$, which may be thought of as a scaling velocity for the eddy flux. Rearranging Eq. (16) we find that

$$v_e = \frac{A_I}{l} = \frac{\tau}{\rho f \Delta\eta} - \frac{l_s}{T_{\mathrm{restore}}}. \quad (21)$$

When this is plotted on a log scale versus $\Delta\eta$ (Fig. 15), several limits are revealed. First, assuming constant $l$, the Gent–McWilliams parameterization would predict a constant value for $A_I/l$, which is not seen in the simulations. By contrast, the Visbeck et al. (1997) parameterization predicts a linear dependence on $\Delta\eta$, which describes the simulations for all but the largest values.

When $\Delta\eta$ is large, the slope seems to increase (as would be expected from saturation arguments), and the Held–Larichev parameterization performs better than the other two.

Although the bulk parameterizations do capture some of the key features of the dependence of the density structure on wind stress, they do not capture the correct spatial structure of the flux. As can be clearly seen in Fig. 13, the cross-Bernoulli-gradient eddy flux in the eddy-resolving model is strongly asymmetric about the ridge, with a strong zonal component. The local eddy parameterizations (Figs. 16a and 16b) capture the fact

that the eddy flux is associated with the ridge and has a strong zonal component. However, they all predict that the fluxes are nearly symmetric about the ridge with the largest fluxes *upstream* of the ridge. They also predict that the flux on the downstream side of the ridge is close to the flanks of the ridge, whereas the fluxes are strongest farther downstream in the eddy-resolving simulations.

It might be argued that the spatial distribution of the eddy fluxes is not essential for a successful parameterization, provided that the integrated fluxes across a mean streamline are accurately predicted. The integrated parameterized flux across mean streamlines, however, must match the eddy fluxes or the parameterized mean state will differ from the true mean state by an amount determined by the mismatch. For each of the three parameterizations, the coefficients required to reproduce the transient eddy flux across about 25 contours from each simulation are shown in Fig. 17. The time-mean fields are used to evaluate each parameterization—this is roughly equivalent to removing the eddies while retaining all the details of the mean state. The variations between contours within a simulation and between simulations are robust representations of the varying conditions that the contours sample; with an average over 2500 days, the variations are not a result of inadequate sampling periods. A successful, complete parameterization would have a nearly constant coefficient over the contours.

The required coefficient with the Gent et al. (1995) parameterization exhibits dramatic variations (Fig. 17a), even over a factor of 3 within a single simulation. Not surprisingly, there is an unambiguous requirement for a larger coefficient with increasing eddy strength. With a constant coefficient, the Gent et al. (1995) parameterization is clearly inadequate for describing the eddy fluxes in the simulations described here.

The Held–Larichev parameterization also requires an extremely large variation (by a factor of 20) of its coefficient (Fig. 17c), and it is evident that in the cases with weaker eddy fluxes it does not capture the dependency of the eddy fluxes on the mean state. With the localization of the strongest eddy activity near the topography, especially with the weaker eddy fluxes and the Held–Larichev assumption of mature beta-plane turbulence, this failure is perhaps not surprising. But in the cases with more vigorous eddy activity, the range of required coefficients collapses substantially, perhaps because the assumptions underlying this parameterization are more appropriate in these cases.

The Visbeck et al. (1997) parameterization is the most promising one for these simulations. However, it still exhibits a disturbingly large variation (by a factor of 3 for contours with significant eddy fluxes) of the diagnosed coefficient (Fig. 17b). The small values of the coefficient with small eddy fluxes and the rapid increase in the coefficient as $R$ approaches 1 are a possible indication of the role of planetary vorticity gradients in
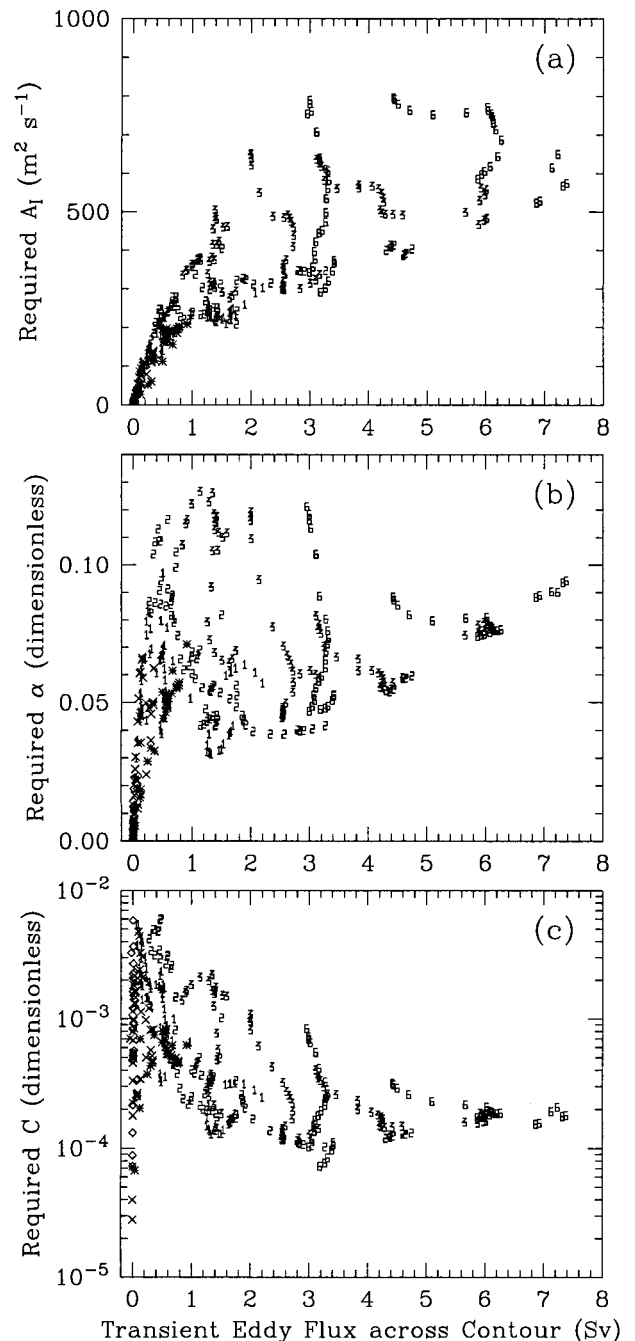


FIG. 17. The coefficients that would be required for the parameterizations of (a) Gent et al. (1995), (b) Visbeck et al. (1997), and (c) Held and Larichev (1996) to reproduce the observed transient eddy fluxes across time-mean Bernoulli function contours, plotted against the transient eddy mass flux across that contour. The parameterized fluxes are based on the time-mean, but otherwise unsmoothed, fields. About 25 contours, which are evenly spaced 1/2° apart at 0° and which transit the entire basin without closing primarily through the damping regions, are used from each of the simulations. The symbols indicate the value of $R$ in the simulations, either as a rounded number or asterisk for $R = 0.6$, cross for $R = 0.4$, or diamond for $R = 0.2$. The averages are taken over 2500 days and are essentially indistinguishable if a different period is chosen. Note the logarithmic scale in (c).

stabilizing the flow, an effect not present in the $f$-plane cases upon which this parameterization is based. The points with the largest required coefficient come from paths that are only slightly deflected over the topography, and on which the intense eddy activity is limited to a small portion of the path length. The inhomogeneity of the flow and the displacement of the greatest eddy activity from the most unstable regions is most prominent on these contours. At large values of the eddy flux, there is apparently a positive tendency of the coefficient with increasing eddy flux. This would be expected if eddy saturation becomes significant. Although the Visbeck et al. (1997) parameterization does generally capture the overall dependence of the eddy activity on the flow strength once there is significant eddy activity, it clearly is inadequate for portraying important nonlocal aspects of the eddy activity, eddy saturation, or the stabilizing effect of the planetary vorticity gradients on weak flows.

These simulations have demonstrated clear deficiencies in several recent parameterizations, both in a bulk formulation and in a local formulation. The use of these parameterizations in a simulation would likely lead to a qualitatively different mean state from that which emerges when eddy activity is well resolved. These simulations would seem to suggest that a Lagrangian parameterization of the eddy effects might be necessary to describe the distribution of eddy fluxes. This would require, first, solution of an equation for baroclinic eddy energy including eddy growth, downstream advection by the large-scale flow, and self-propagation of eddies and, second, a parameterization of the eddy effects based (for example) on that eddy intensity and a tendency for eddies to homogenize PV.

## 5. Discussion

This paper has shown that transient eddies play a key role in setting the transport of a wind-forced current in a reentrant channel. The role played by the eddies, however, is not simple. The eddies generate interfacial form stresses that transfer the surface stress to the deep layer. The eddies are also associated with the partial homogenization of potential vorticity in the lower layer, resulting in more pronounced stationary eddies. The stationary eddies are associated with strong zonal internal interface height gradients, across which transient eddies fluxes can return the Ekman flux. The close interconnection between stationary and transient eddies means that the path as well as the transport of the mean current depends on the wind stress.

This research raises some clear questions about how well local parameterizations of eddy transport that depend solely on the local density structure (such as those proposed by Gent and McWilliams 1990; Held and Larichev 1996; Visbeck et al. 1997) will be capable of reproducing the eddy fluxes and their effect on the mean flow. Such local theories will not capture the asymmetry

of the eddy energy or of eddy fluxes around topography. This failure may be related to the relatively poor correlation between such parameterizations and eddy fluxes found in models (Bryan et al. 1999). Local, isopycnal-slope-based theories may also have trouble in reproducing the dependence of the eddy energy on wind stress once the current is saturated.

The model presented here is motivated by our desire to explain the dependence of the circumpolar current and thermohaline overturning on wind stress. While the model is clearly unrealistic in many ways, one can draw certain important conclusions from it. First, in the present ocean approximately half of the northward Ekman flux is injected into the thermocline as AAIW implying an $R$ of approximately 1. The results from this paper suggests that changes in the Southern Ocean wind stress will be compensated more by eddies than by northern overturning, but that both will probably play a role. Second, this paper points out yet again the important role of topographic features in determining the transport of the circumpolar current, as they have a profound effect on both the stationary and transient eddy field. Any attempts to measure eddy fluxes should focus on areas downstream of topography.

The results here clearly suffer from a number of deficiencies. The interface height damping is clearly a very crude representation of the diabatic forcing of the real ocean. The channel is much wider, the radius of deformation much larger, the stratification much sharper, and the topography much simpler than in the real world. More realistic experiments are now being carried out as part of the Modeling Eddies in the Southern Ocean project at GFDL. These simulations use two very different primitive equation ocean models [HIM, which is used here, and the geopotential coordinate MOM (Pacanowski and Griffies 1999)], subject to the same suite of different values of surface forcing. While preliminary runs are being carried out at the same resolution as the FRAM (Webb et al. 1991), much finer resolution simulations will be carried out over the next few years. It is our hope that these runs will help us to a deeper understanding of the complex interplay between topography, transient eddies, and buoyancy forcing that sets the strength of the world's largest ocean current and has implications for the density structure of the entire ocean.

## REFERENCES

Arakawa, A., and Y.-J. G. Hsu, 1990: Energy conserving and potential enstrophy dissipating schemes for the shallow water equations. *Mon. Wea. Rev.,* **118,** 1960–1969.

Bryan, K., J. K. Dukowicz, and R. D. Smith, 1999: On the mixing coefficient in the parameterization of bolus velocity. *J. Phys. Oceanogr.,* **29,** 2442–2456.

de las Heras, M. M., and R. Schlitzer, 1999: On the importance of intermediate water flows for the global ocean overturning. *J. Geophys. Res.,* **104,** 15 515–15 536.

Döös, K., and D. J. Webb, 1994: The Deacon cell and the other meridional cells of the Southern Ocean. *J. Phys. Oceanogr.,* **24,** 429–442.

Gent, P., and J. C. McWilliams, 1990: Isopycnal mixing in ocean models. *J. Phys. Oceanogr.,* **20,** 150–155.

——, J. Willebrand, T. J. McDougall, and J. C. McWilliams, 1995: Parameterizing eddy-induced transports in ocean circulation models. *J. Phys. Oceanogr.,* **25,** 463–474.

——, W. G. Large, and F. O. Bryan, 2001: What sets the mean transport through Drake Passage? *J. Geophys. Res.,* **106,** 2693–2712.

Gille, S. T., 1997: The Southern Ocean momentum balance: Evidence for topographic effects from numerical model output and altimeter data. *J. Phys. Oceanogr.,* **27,** 2219–2232.

——, and K. A. Kelly, 1996: Scales of spatial and temporal variability in the Southern Ocean. *J. Geophys. Res.,* **101,** 8759–8773.

Gnanadesikan, A., 1999: A simple predictive model for the structure of the oceanic pycnocline. *Science,* **283,** 2077–2079.

——, and R. W. Hallberg, 2000: The relationship of the Circumpolar Current to Southern Hemisphere winds in coarse-resolution models. *J. Phys. Oceanogr.,* **30,** 2013–2034.

Griffies, S. M., 1998: The Gent–McWilliams skew flux. *J. Phys. Oceanogr.,* **28,** 831–841.

Hallberg, R., 1997: Stable split time stepping schemes for large-scale ocean modeling. *J. Comput. Phys.,* **135,** 54–65.

——, and P. B. Rhines, 1996: Buoyancy-driven circulation in an ocean basin with isopycnals intersecting the sloping boundary. *J. Phys. Oceanogr.,* **26,** 913–940.

Held, I. M., and V. D. Larichev, 1996: A scaling theory for horizontally homogeneous baroclinically unstable flow on a beta-plane. *J. Atmos. Sci.,* **53,** 946–952.

Hirst, A. C., 1999: Determination of water component age in ocean models: Application to the fate of North Atlantic deep water. *Ocean Modelling,* **1,** 81–94.

Hsu, Y.-J. G., and A. Arakawa, 1990: Numerical modeling of the atmosphere with an isentropic vertical coordinate. *Mon. Wea. Rev.,* **118,** 1933–1959.

Hughes, C. W., M. P. Meredith, and K. J. Heywood, 1999: Wind-driven transport fluctuations through Drake Passage: A southern mode. *J. Phys. Oceanogr.,* **29,** 1971–1992.

Ivchenko, V. O., K. J. Richards, and D. P. Stevens, 1996: The dynamics of the Antarctic Circumpolar Current. *J. Phys. Oceanogr.,* **26,** 753–774.

Johnson, G. C., and H. Bryden, 1989: On the strength of the Circumpolar Current. *Deep-Sea Res.,* **36,** 39–53.

Kalnay, E., and Coauthors, 1996: The NCEP/NCAR 40-Year Reanalysis Project. *Bull. Amer. Meteor. Soc.,* **77,** 437–471.

Killworth, P. D., and M. M. Nanneh, 1994: Isopycnal momentum budget of the Antarctic Circumpolar Current in the Fine Resolution Antarctic Model. *J. Phys. Oceanogr.,* **24,** 1201–1223.

Krupitsky, A., V. M. Kamenkovich, N. Naik, and M. A. Cane, 1996: A linear equivalent barotropic model of the Antarctic Circumpolar Current with realistic coastlines and bottom topography. *J. Phys. Oceanogr.,* **26,** 1803–1824.

Lee, M.-M., D. P. Marshall, and R. G. Williams, 1997: On the eddy transfer of tracers: Advective or diffusive? *J. Mar. Res.,* **55,** 483–505.

MacCready, P., and P. B. Rhines, 2001: Meridional transport across a zonal channel: Topographic localization. *J. Phys. Oceanogr.,* **31,** 1427–1439.

MacDonald, A., 1998: The global ocean circulation: A hydrographic estimate and regional analysis. *Progress in Oceanography,* Vol. 41, Pergamon, 281–382.

Marshall, J., D. Olbers, H. Ross, and D. Wolf-Gladrow, 1993: Potential vorticity constraints on the dynamics and hydrography of the Southern Ocean. *J. Phys. Oceanogr.,* **23,** 465–487.

McWilliams, J. C., W. H. Holland, and J. H. S. Chow, 1978: A description of numerical Antarctic Circumpolar Currents. *Dyn. Atmos. Oceans,* **2,** 213–291.

Munk, W. H., and E. Palmén, 1951: Note on the dynamics of the Antarctic Circumpolar Current. *Tellus,* **3,** 53–55.

Olbers, D., and C. Völker, 1996: Steady states and variability in oceanic zonal flows. *Decadal Climate Variability,* D. L. T. Anderson and J. Willebrand, Eds., NATO ASI Series I, Vol. 44, Springer Verlag, 407–433.

Orsi, A. H., T. Whitworth III, and W. D. Nowlin, 1995: On the meridional extent and fronts of the Antarctic Circumpolar Current. *Deep-Sea Res. I,* **42,** 641–673.

Pacanowski, R., and S. M. Griffies, 1999: The MOM3 Manual. GFDL Ocean Group Tech. Rep. No. 3, 704 pp.

Pedlosky, J., 1987: *Geophysical Fluid Dynamics.* Springer-Verlag, 710 pp.

Rhines, P. B., 1977: The dynamics of unsteady currents. *The Sea,* Vol. 6: *Marine Modeling,* E. Goldberg, Ed., Wiley, 189–318.

——, and W. R. Young, 1982: A theory of wind-driven circulation. I. Mid-ocean gyres. *J. Mar. Res.,* **40** (Suppl.), 559–596.

Schmitz, W. J., 1995: On the interbasin-scale thermohaline circulation. *Rev. Geophys.,* **33,** 151–173.

Straub, D., 1993: On the transport and angular momentum balance of channel models of the Antarctic Circumpolar Current. *J. Phys. Oceanogr.,* **23,** 776–782.

Tansley, C., and D. Marshall, 2001: On the dynamics of wind-driven circumpolar currents. *J. Phys. Oceanogr.,* **31,** 3258–3273.

Toggweiler, J. R., and B. Samuels, 1993: New radiocarbon constraints on the upwelling of abyssal water to the ocean's surface. *The Global Carbon Cycle,* M. Heimann, Ed., Springer-Verlag, 333–365.

——, and ——, 1995: Effect of Drake Passage on the global thermohaline circulation. *Deep-Sea Res.,* **42,** 477–500.

——, and ——, 1998: On the ocean's large-scale circulation near the limit of no vertical mixing. *J. Phys. Oceanogr.,* **28,** 1832–1852.

Treguier, A. M., and J. C. McWilliams, 1990: Topographic influences on the Antarctic Circumpolar Current. *J. Phys. Oceanogr.,* **20,** 321–343.

Trenberth, K., J. G. Olson, and W. G. Large, 1989: A global ocean wind stress climatology based on ECMWF analyses. NCAR Tech. Note NCAR/TN-338+STR, 93 pp.

Visbeck, M., J. Marshall, T. Haine, and M. Spall, 1997: Specification of eddy transfer coefficients in coarse-resolution ocean circulation models. *J. Phys. Oceanogr.,* **27,** 381–402.

Völker, C., 1999: Momentum balance in zonal flows and resonance of baroclinic Rossby waves. *J. Phys. Oceanogr.,* **29,** 1666–1681.

Wang, L., 1994: A linear homogeneous channel model for topographic control of the Antarctic Circumpolar Current. *J. Mar. Res.,* **52,** 649–685.

——, and R. X. Huang, 1995: A linear homogeneous model of wind-driven circulation in a β-plane channel. *J. Phys. Oceanogr.,* **25,** 587–603.

Warren, B., J. LaCasce, and P. A. Robbins, 1996: On the obscurantist physics of "form drag" in theorizing about the Circumpolar Current. *J. Phys. Oceanogr.,* **26,** 2297–2301.

Webb, D. J., P. D. Killworth, D. Beckles, B. A. de Cuevas, R. Offiler, and M. Rowe, 1991: An eddy-resolving model of the Southern Ocean. *Eos, Trans. Amer. Geophys. Union,* **72,** 169–175.

Whitworth, T., III, W. D. Nowlin, and S. J. Worley, 1982: The net transport of the Antarctic Circumpolar Current through Drake Passage. *J. Phys. Oceanogr.,* **12,** 960–971.

Witter, D. L., and D. B. Chelton, 1998: Eddy-mean flow interaction

in zonal oceanic jet flow along zonal ridge topography. *J. Phys. Oceanogr.,* **28,** 2019–2039.

Wolff, J.-O., E. Maier-Raimer, and D. J. Olbers, 1991: Wind-driven flow over topography in a zonal $\beta$-plane channel: A quasi-geo-strophic model of the Antarctic Circumpolar Current. *J. Phys. Oceanogr.,* **21,** 236–264.

Wunsch, C., 1998: The work done by the wind on the oceanic circulation. *J. Phys. Oceanogr.,* **28,** 2332–2340.